communications materials

A Nature Portfolio journal

Article

https://doi.org/10.1038/s43246-026-01261-3

Eco-friendly water-synthesis of lead-free Cs2AgBiBr6 perovskites

Check for updates

Paola De Padova[1,2] ✉, Bruno Olivieri[3], Carlo Ottaviani[1], Osamu Kubo[4], Sofia Caretto[5], Angelo De Paolis[5], Annalisa Paradiso[5], Paola Prete[6,7], Nico Lovergine[6], Filippo Ruggiero[1], Amanda Generosi[1], Barbara Paci[1], Rodrigo Szostak[8], Francisco Mateus Cirillo da Silva[8], Hélio C. N. Tolentino[8], Tulio Costa Rizuti da Rocha[8], Luiz Gustavo de Freitas Borges[8], Flavio Cesar Vicentin[8] & Aldo Di Carlo[1]

The synthesis of lead-free $Cs_2AgBiBr_6$ perovskite is a huge challenge within the framework of the new emergent full-inorganic materials, with the aim of being employed as sensitive layers for a new generation of solar cells and/or optoelectronic devices.Here we report an innovative eco-friendly method for the preparation of $Cs_2AgBiBr_6$ perovskite, obtained both by "wet" and "dry" CsBr, AgBr, and $BiBr_3$ precursor salts, in a fully hydro-solution liquid process, free of chemical solvents. $Cs_2AgBiBr_6$ powders and $Cs_2AgBiBr_6$ lead-free perovskite nanocrystal films have been realised and investigated for electronic, structural, and optical properties. X-ray diffraction revealed that powders and/or perovskite films obtained in a water bath belong to the cubic phase, symmetry group *Fm-3m*, as revealed by scanning electron microscopy as tetrahedral nanocrystal morphology. Energy gaps of about 2.10 and 2.60 eV are evidenced by synchrotron radiation valence band photoemission spectroscopy, photo-cathodo-luminescence, and optical measurements. Core levels x-ray photoemission and synchrotron radiation x-ray fluorescence spectroscopies give insights on $Cs_2AgBiBr_6$ perovskite formation in water-process solution.

Perovskites, in their simplest chemical formulation, have an ABX_3 type chemical formula, for both hybrid or fully inorganic compounds[1–4]; in which A represents the cation, as, for example, methylammonium (MA^+) (CH_3NH_3), formamidinium (FA^+), and/or other monovalent organic cations, for hybrid, and rubidium (Rb+), caesium (Cs+) for inorganic systems; B is the metal cation, with 2+ coordination, very often, lead (Pb^{2+}), indeed X^- is the halogen anion, chlorine (Cl^-), bromine (Br^-), and/or iodine (I^-), with coordination 3 in the ABX_3 perovskite structure[1–4].

The significance of employing perovskites lies in their potential to enable a new and emerging class of photovoltaic technologies, with high sunlight energy conversion, low-cost synthesis, and suitability for a broad range of optoelectronic applications, largely due to the easy tunability of their band gap.

Following the seminal discovery by Kojima et al. in 2009[5], in which two organometallic lead halide perovskites, $CH_3NH_3PbBr_3$ and $CH_3NH_3PbI_3$, were utilized as photo-absorbers for photovoltaic (PV) solar cells—with initial power conversion efficiencies (PCEs) of 3.13% and 3.81%, respectively[5]—the field has experienced remarkable advancements. Single-junction devices have since achieved a PCE of 27%, while perovskite/silicon tandem devices have reached a record PCE of 34.6%[6]. These breakthroughs have paved the way for perovskite-based technologies to become increasingly competitive with conventional silicon-based PV systems, including configurations that integrate both silicon and perovskite in a tandem configuration[3].

Due to the toxicity of lead-based compounds and the limited long-term stability of hybrid organic–inorganic perovskites[7,8], their use in human-centred and commercial applications should be restricted. Consequently, the demand for alternative materials has been rapidly increasing. At the same time, this issue has also stimulated a significant academic and technological interest in developing more sustainable approaches.

One strategy is to move to the development/investigation of Pb-free perovskites, replacing, for example, lead with the less toxic tin, (Sn^{2+})[8], in

[1]Consiglio Nazionale delle Ricerche, Istituto di Struttura della Materia, Roma, Italy. [2]INFN-LNF, Frascati, CNR, Italy. [3]Consiglio Nazionale delle Ricerche, Istituto di Scienze dell'Atmosfera e del Clima, Roma, Italy. [4]University of Gifu Engineering, Gifu, Japan. [5]Consiglio Nazionale delle Ricerche, Istituto Scienze delle Produzioni Alimentari, Lecce, Italy. [6]Dipartimento di Ingegneria dell'Innovazione, Università del Salento, Lecce, Italy. [7]Consiglio Nazionale delle Ricerche, Istituto per la Microelettronica e Microsistemi, Lecce, Italy. [8]Brazilian Synchrotron Light Laboratory (LNLS), Brazilian Center for Research in Energy and Materials (CNPEM), Rua Giuseppe Máximo Solfaro, Campinas, São Paulo, Brazil. ✉e-mail: depadova@ism.cnr.it

order to increase the stability, durability over time and high power-light conversion efficiency of the active layer based on the perovskites.

Another successful approach is to develop combinations of completely inorganic and lead-free compounds such as $A_2BB'X_6$ (X = Br, Cl, I) halide double perovskite-like compounds, based on Bi and Ag. These compounds have recently been synthesized, exhibiting suitable band gaps in the entire visible spectrum, representing promising alternatives to Pb-hybrid halide perovskites[9–11]. In 2016, Slavney et al. reported the first synthesis of a non-toxic and stable single crystal of $Cs_2AgBiBr_6$[12] perovskite, which crystallizes in the *Fm-3m* cubic space group at room temperature (RT)[12], and subsequently they were extensively explored[13].

What makes the development of the $Cs_2AgBiBr_6$ perovskite extremely appealing is its chemical-physical property. A surprising peculiarity is the large room temperature (RT) photoluminescence (PL) lifetime, around 660 ns[12], much higher than the value (170 ns) found for high-quality $MAPbBr_3$[4], and closest to that obtained in $MAPbI_3$(Cl) films (736 ns)[14,15]. Noteworthy, the decay of the PL curve reported by Slavney et al.[12], showed that the majority of carriers can recombine through this long-lived process, presenting differences of only 6% between powder and single-crystal samples. This suggests that the presence of surface defects or spurious sites does not constitute an impediment to photovoltaic performance.

Fully inorganic $Cs_2AgBiBr_6$ perovskite presents excellent thermal stability, with mass loss only at temperatures higher than 430 °C[12], no evidence of decomposition in the ambient atmosphere was observed for a long period of time (240 days)[16]. Furthermore, this quaternary compound, $Cs_2AgBiBr_6$, does not exhibit binary and/or ternary secondary phases, usually, formed at RT, but a single face-centred-cubic phase. Only extreme physical conditions, such as temperature around 122 K[17], or pressure of above ~2.3 GPa[18], (up to 3.2 GPa)[19], favour the crystallization into a tetragonal phase (space group I/4 m), with reduced bandgap.

The silver-bismuth halide double perovskite exhibits an indirect bandgap of 1.95 eV[12], which is, among other properties, particularly important for Si coupling in a tandem solar cell. However, this perovskite displays a very large bandgap tunability. Impurity doping, by alloying diluted Tl atoms[20], has demonstrated for $Cs_2AgBiBr_6$ perovskite a bandgap reduced to 1.45 eV, from an indirect bandgap of 1.95 eV, which becomes direct, without dramatic structural change, thus being similar to that of $(CH_3NH_3)PbI_3$, by defect-induced band-edge modification, suitable for visible light absorption[20]. The bandgap engineering of lead-free double perovskite $Cs_2AgBiBr_6$ is also obtained by introducing In or Sb atom doping, leading to a modulation and/or reduction (of 0.41 eV) of the bandgap, as a function of the atomic species, drastically modifying the appearance of the perovskite colour[21]. Lead-free $Cs_2AgBiBr_6$ perovskite with decreased bandgap was, indeed, obtained by controlling the crystal growth temperature/speed, reaching a decreased bandgap of 1.72 eV (reduction of 0.26 eV), under ambient conditions[16]. First-principles calculations indicated that enhanced Ag–Bi disorder could influence band structure, decreasing the band gap[16].

Noteworthy, a thermochromic effect has been observed in the lead-free double perovskite $Cs_2AgBiBr_6$, both in single crystal and films, as a reversible temperature depending on bandgap change[22]. First-principles molecular dynamics simulations have revealed the presence of Ag–Br and Bi–Br bond lengths anharmonic fluctuations at higher temperatures, which are associated with both electron–phonon coupling and spin–orbit coupling effect, which are the main responsible for this thermochromic process[22].

The lead-free $Cs_2AgBiBr_6$ perovskite has been successfully applied in optoelectronic devices[23–27], as well as active layer for photovoltaic devices[28,29], for which, in particular, the calculated Shockley-Queisser efficiency limit[30] predicts a value high as ~16%[31], allowing to its power conversion energy (PCE) to increase from about 1.1% (with V_{oc} of 1.06 V)[32], to about/or exceeding the PCE of 3%[23,29,33,34] in a short period of time[34,35]. It is worth noting that $Cs_2AgBiBr_6$, due to its large bandgap, is a suitable candidate for applications in tandem solar cells as, it was already shown for methylammonium lead bromide, which has even a quite larger bandgap of 2.3 eV[36], and already in single-crystal X-ray detectors with a low detection limit, as low as 59.7 nGyair s^{-1}, similar to the latest record performed by $CH_3NH_3PbBr_3$ single crystals (0.036 μGyair s^{-1}) has been realised[24].

Usually, large crystals of $Cs_2AgBiBr_6$ have been obtained from a solution of HBr stoichiometric CsBr, AgBr, and $BiBr_3$ salts[12,22,24,37,38], and nanocrystals, with side length of ~8 nm, from colloidal procedure, combining caesium, silver and bismuth acetate, $Cs(OAc)^+Ag(OAc)^+Bi(OAc)$, with injection of trimethylsilyl (TMSX, X=Br, Cl, I) and successive chemical steps[39,40]. Spin-coated and spray-coated $Cs_2AgBiBr_6$ films have been achieved by solution of $CsBr/AgBr/BiBr_3$ in dimethyl sulfoxide (DMSO)[17,22,23,25,32,33,34] and in DMSO and dimethylformamide (DMF), respectively[41]. In addition, single-source vapour deposition was loaded with $Cs_2AgBiBr_6$ crystals, obtained by chemical preparation, and ground to a yellow powder to deposit thin $Cs_2AgBiBr_6$ films[42].

In this work, we report the synthesis of ordered lead-free double-cation $Cs_2AgBiBr_6$ perovskite powders and films by an in-air hydro liquid process from precursor salts of AgBr, CsBr and $BiBr_3$, completely chemical solvents-free, named, here, *perovskites water-synthesis* process. The procedure comprises preparing stoichiometric (orange perovskite), and sub-stoichiometric (yellow perovskite) mixtures, and no mixing among the salt precursor powders, and a liquid bath of water.

We obtained very stable $Cs_2AgBiBr_6$ perovskites in all prepared mixed and no-mixed powders, "dry", and after the water solution process, "wet", exhibiting a cubic phase, symmetry group *Fm-3m*, as revealed by X-ray diffraction. Energy band gaps of 2.10 eV, and 2.60 eV, were probed by synchrotron radiation valence band and confirmed by photoluminescence, cathodoluminescence, and optical measurements. X-ray core-level photoemission and X-ray synchrotron radiation fluorescence spectroscopies provided details on the mechanism of $Cs_2AgBiBr_6$ perovskite formation in the water-solution process.

Results and Discussion

Panels (a) to (f) of Fig. 1 show the various stages of synthesis of lead-free perovskites, $Cs_2AgBiBr_6$, which were completely produced in an environmentally friendly manner, without chemical solvents, by an innovative procedure, described hereafter. The images on the left show the perovskite, called orange $Cs_2AgBiBr_6$, while the images on the right show the perovskite named yellow $Cs_2AgBiBr_6$.

Figure 1b, e show the orange and yellow powders, obtained by simply mixing with a spatula or/and using a pestle the three precursor salts, CsBr (white in colour), AgBr (bluish-greenish in colour), and $BiBr_3$ (yellowish-greenish in colour), shown in (a), in stoichiometric (2:1:1) and sub-stoichiometric (1:1:1) in molar weights concentrations, for orange and yellow respectively; while in Fig. 1c, f, the perovskite powders are dissolved in H_2O filtered, bi-distilled and deionized water, with conductivity of about 18 M ohm, or ultrapure, continuing to maintain their different and strong colour, of orange and yellow.

Once the aqueous liquid solution is obtained, drops of liquid are dropped and spread on substrates, such as glass and/or indium tin oxide/glass (ITO), TiO_2/fluorine doped TiO_2/glass, to create thin films, as shown in panels (d) and (g) of Fig. 1. The drying process and the entire perovskites production process take place under ambient air conditions.

The colour reported in the images of Fig. 1b–g, indicates the successful synthesis of $Cs_2AgBiBr_6$ perovskites, similar to those of literature[12,16,21–23,39,42]. However, previously reported syntheses of $Cs_2AgBiBr_6$ perovskites have primarily involved dissolving precursor salts in chemical solvents such as HBr, DMS, as well as DMSO[17,22,23,25–27,32,33,34,41].

To support this observation and to assess the crystal structure of the perovskites, we performed X-ray diffraction (XRD) on the realised samples. Figure 2a reports the XRD pattern of the orange film $Cs_2AgBiBr_6$, named hereafter old-orange $Cs_2AgBiBr_6$, deposited on the ITO layer on glass substrate 2 months before the XRD measurements. Figure 2b shows the XRD spectrum collected on a fresh $Cs_2AgBiBr_6$ sample, obtained from the same powder as old-orange $Cs_2AgBiBr_6$, and measured and dried after 1 hour 24 minutes of its synthesis, of its realization (b). Figure 2c is a drawing of the $Cs_2AgBiBr_6$ cubic crystal structure, *Fm-3m*[12,16,21–23,27,32,40]. Notably, the

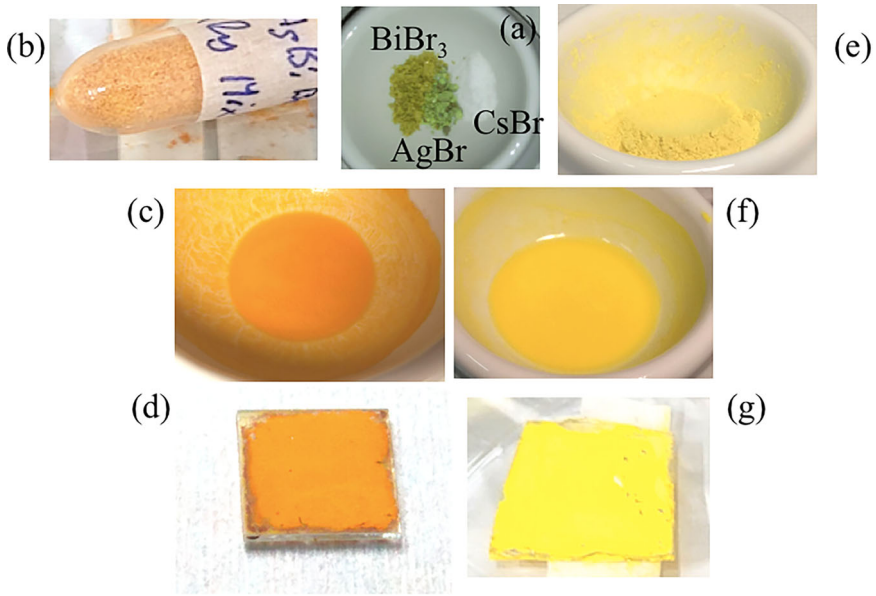


Fig. 1 | Optical images of the orange and yellow $Cs_2AgBiBr_6$ perovskite preparations. a CsBr, AgBr, and $BiBr_3$ precursor salts before mixing, **b**, **e** orange and yellow mixed powders; **c** **d** acquous and dried film of the orange $Cs_2AgBiBr_6$ perovskite; **f**, **g** liquid and film of the yellow $Cs_2AgBiBr_6$ perovskite.

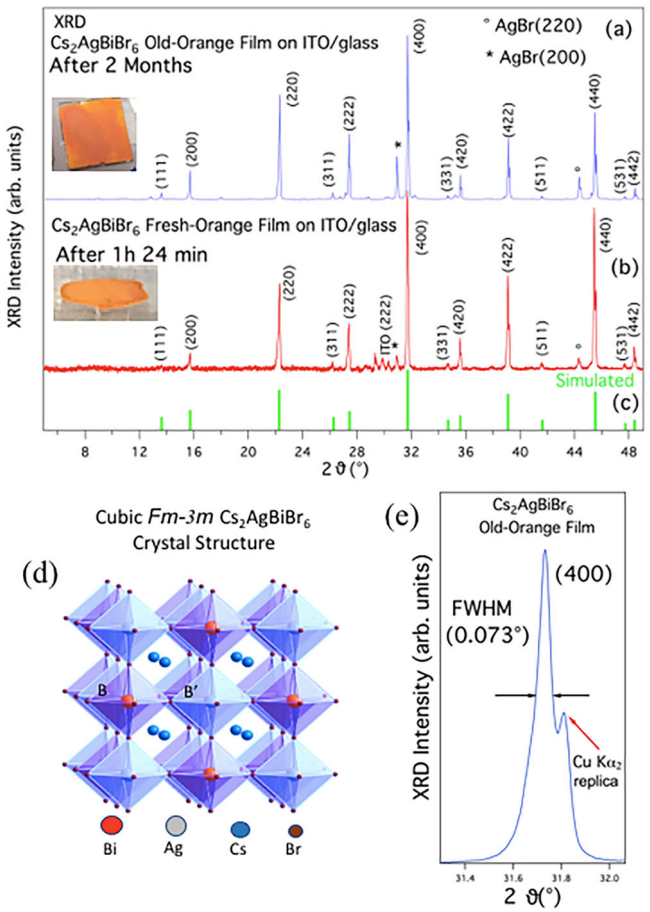


Fig. 2 | XRD patterns of orange $Cs_2AgBiBr_6$ perovskite films after air aging and as deposited, their optical photos and atomic structure. a old-orange measured after 2 months, and **b** 1 h 24 min fresh-orange $Cs_2AgBiBr_6$ perovskite films; **c** simulated XRD $Cs_2AgBiBr_6$ perovskite structure, in green; **d** cubic *Fm-3m* crystal structure; **e** is a detail of **a**, where the black double arrows mark the FWHM of the (400) peak, and the red arrow its replica. The Bi, Ag, Cs and Br atoms are represented by red, silver, blue and brown colours. The optical images of old- and fresh-$Cs_2AgBiBr_6$ samples are also reported.

double-cation $Cs_2AgBiBr_6$ perovskite at RT, usually crystalizes in the cubic (*Fm-3m*) crystal structure, with a large lattice parameter a = 11.25 Å, where the Ag^+ and Bi^{3+} ions occupy the B and B′ sites, see Fig. 2d, in the ordered double-perovskite lattice with slightly different metal-bromide bond lengths. The structure is composed of alternate connected corner of $[AgBr_6]^{5-}$ and $[BiBr_6]^{3-}$ octahedra, in all three directions, with the ion Cs^+ that occupies the centre of four $AgBr_6$ and $BiBr_6$ octahedra units, as shown in Fig. 2d. This quaternary compound can undergo a crystal phase transition, by lowering its crystal symmetry, from a cubic face-centred to a tetragonal structure (space group *I4/m*), by simply applying a low temperature, such as 122 K[17], and/or a high pressure of about 2.3 GPa[18].

The XRD reflection peaks of both old- and fresh- orange $Cs_2AgBiBr_6$ films are indexed in Fig. 2a, b as the (111), (200), (220), (311), (222), (400), (331), (420), (422), (511), (440), (531), and (442), located at 13.598°, 15.730°, 22.282 °, 26.172 °, 27.378 °, 31.715 °, 34.627 °, 35.579 °, 39.094 °, 41.579°, 45.453 °, 47.653 °, and 48.381 °, respectively, in good agreement with previous literature[12,18,21,22,41–44]. The simulated pattern of these XRD reflections, Fig. 2c, performed by using the HighScore (Panalytical) programme, were found at values: 13.607°, 15.725°, 22.309 °, 26.223 °, 27.411 °, 31.756 °, 34.691 °, 35.622 °, 39.154 °, 41.636°, 45.525 °, 47.738 °, and 48.458 °, in perfect agreement with experimental results. No further differences are found in the two spectra, related to the crystallographic signature. These remarkable results highlight the structural stability of both perovskite films and powder, intentionally stored in air, in a vial, to test their resistance against aging.

The spectrum of Fig. 2e reports the detail of the (400) reflection of the old-orange $Cs_2AgBiBr_6$ perovskite spectrum of Fig. 2a, exhibiting a FWHM of 0.073°. Its replica, shifted by 0.072 °, due to the presence of Cu $K\alpha_2$ X-ray (λ = 1.54439 Å) is clearly visible[45].

To our best knowledge this full width half maximum (FWHM) is the narrowest reported so far, even in $Cs_2AgBiBr_6$ single crystals, where the value of the order of 0.2113° for the (220) reflection was measured, then lowered to 0.1297° by adding the phenylethylamine bromide (PEABr) to the precursor salts of the $Cs_2AgBiBr_6$ perovskite, allowing the production of a single crystal $Cs_2AgBiBr_6$ with a higher crystalline order[44].

This $Cs_2AgBiBr_6$ perovskite can be considered pure, showing no additional spurious peaks, although two small peaks labelled with "*" and "∘", located at 30.913° and 44.292° and attributed to (200) and (220) of AgBr, respectively, are present[23], as well as the (222) reflection of ITO from the substrate.

Another noteworthy feature of our synthesized $Cs_2AgBiBr_6$ perovskite is its remarkable stability in terms of colour and optical properties, which is

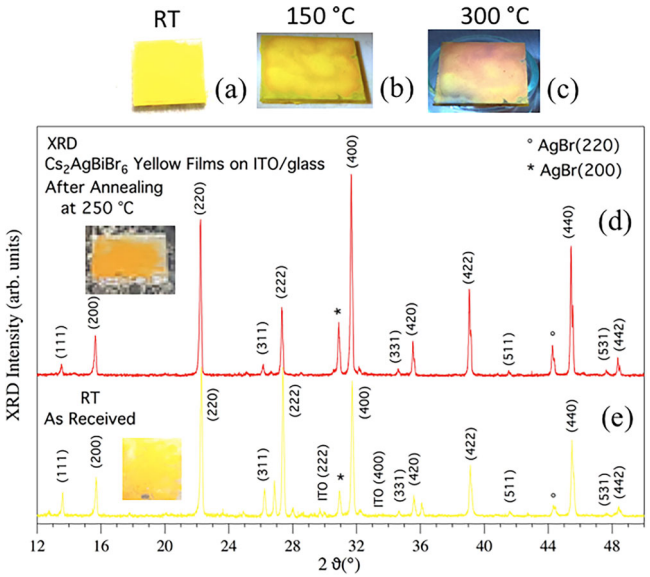


Fig. 3 | Optical images of yellow $Cs_2AgBiBr_6$ perovskite films and XRD patterns of yellow $Cs_2AgBiBr_6$ perovskite films. a as yellow film deposited at RT, **b** annealed at 150 °C for 5 min; and **c** annealed at 300 °C for 5 min. **d**, **e** show the XRD patterns of yellow $Cs_2AgBiBr_6$ perovskite films at RT, and 250 °C, including their optical images: **d** yellow film at RT, and **e** at T = 250 °C.

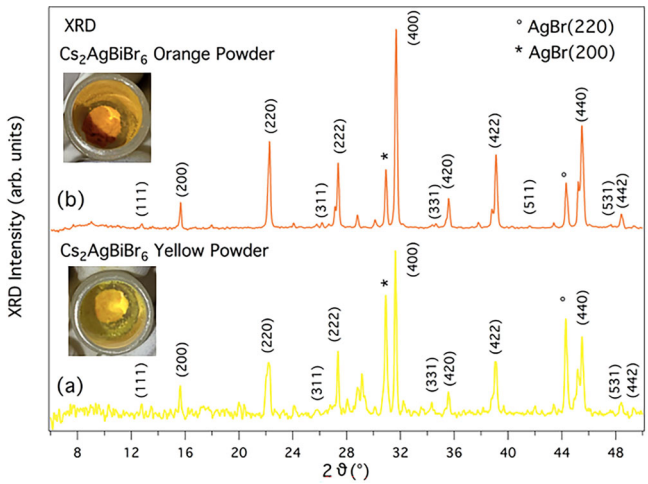


Fig. 4 | XRD patterns of $Cs_2AgBiBr_6$ powders. a orange, **b** yellow powders, and their optical images.

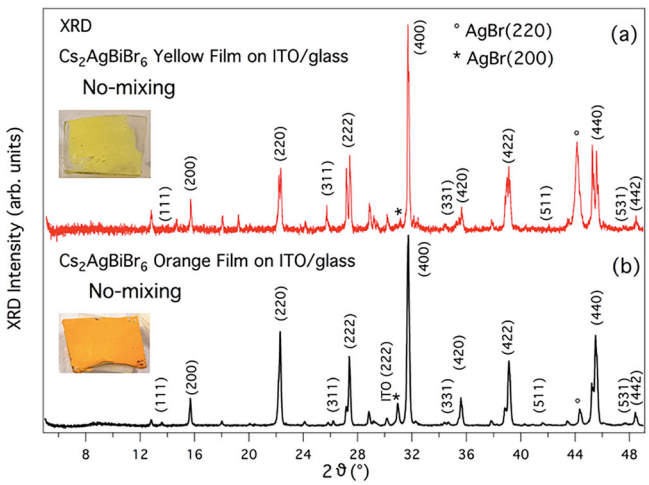


Fig. 5 | XRD patterns of yellow and orange $Cs_2AgBiBr_6$ films obtained without mixing the precursor salts before adding water. a yellow, and **b** orange films with their optical images.

consistently observed whether in powder form, dissolved in water (H_2O), and/or deposited as thin films. XRD analyses, as shown, conducted days and even several months/years after synthesis revealed no signs of degradation, showing XRD patterns, quite identical to those initially recorded.

Noteworthy, therefore, that the use of water alone, without the further addition of chemical solvents, to dissolve $Cs_2AgBiBr_6$ in liquid, not only produces the aforementioned perovskite, but also keeps it stable for a long time, even after drying, dispelling the prejudice that the eventual presence of oxygen/H_2O may not only not form the perovskite, but may even deteriorate it. This fact makes this in liquid process, in water, simple and at the same time remarkably convenient for the development of totally "clean" materials, free of lead, and in the absence of chemical solvents or acids. It should also be noted that after drying, the $Cs_2AgBiBr_6$ perovskite layers can be "scraped" to obtain even more finely ground powders, without any use of ball milling equipment. This further procedure has been validated by the authors, who obtained diffraction patterns of the cubic phase of the perovskite $Cs_2AgBiBr_6$, extremely ordered and pure, such as those shown in Fig. 2, in which it can be noted that H_2O promotes the crystallization formation of the $Cs_2AgBiBr_6$ perovskites.

We now turn to the XRD study of the perovskite produced with substoichiometry of the precursor salts, called yellow $Cs_2AgBiBr_6$, see Fig. 1e–g. Figure 3 reports the images of yellow $Cs_2AgBiBr_6$ films, as-deposited at RT (a), and after heating for 5 minutes at temperatures of 150 °C (b), and 300 °C (c), respectively. Image (b), compared to (a), shows the onset of colour change, remaining yellow but starting the transition to orange; while the image in Fig. 3c clearly turns toward orange. It should be noted that the effect of temperature acts on a yellow $Cs_2AgBiBr_6$ perovskite, even if produced with a different method from the one reported in the present work, in a similar way, in agreement with previous literature[42].

It is clear that in both the two spectra, 3 (d), and 3 (e), the same diffraction peaks are observed in Fig. 2 for the orange $Cs_2AgBiBr_6$ perovskites, apart from a slight difference in the relative intensity of the peaks, also pointing to the cubic crystalline structure of yellow perovskite. Furthermore, it is important to note that, similar to orange perovskite, although slightly wider, for this yellow perovskite, the FWHM is narrow at 0.13° for (a) and 0.11° for (b), exhibiting a high crystal structural order. These are interesting characteristics of the $Cs_2AgBiBr_6$ perovskites, which appear to be very tolerant to defects, maintaining the same crystalline structure but varying their electronic properties[16,26].

To show the crystallinity of both yellow and orange $Cs_2AgBiBr_6$ powders, Fig. 4 reports their XRD patterns. All diffraction peaks belong to the cubic phase.

By applying the Bragg's law ($n\lambda = 2d\sin\vartheta$), where λ(Cu $K_{\alpha 1}$) = 1.54056 Å and $n = 2$ for the (200), from the XRD patterns, we get the cubic $Cs_2AgBiBr_6$ lattice constant values $a_{Cs2AgBiBr6} = 11.327$ Å, for all preparations of perovskite samples so far presented, i. e., the yellow and the orange mixed dried powders, and related films obtained from them after water wetting, and subsequent drying on substrates. This value is also obtained from XRD patterns of Fig. 5, when the $Cs_2AgBiBr_6$ perovskite has been obtained, by weighing the CsBr, AgBr, and $BiBr_3$ precursor salts in a (2:1:1) ratio for orange and (1:1:1) for yellow, placing them separately, without mixing, and adding only water. Remarkably, here, the XRD patterns displayed in Fig. 5 are all in all similar to the previous figures' spectra, where the $Cs_2AgBiBr_6$ perovskite films were synthesised in water after gentle mixing. In this respect, a water process synthesis is hereafter defined. We note that the different intensities of XRD peaks in all patterns reported is mainly due to the different orientations and sizes of the nanocrystals of the

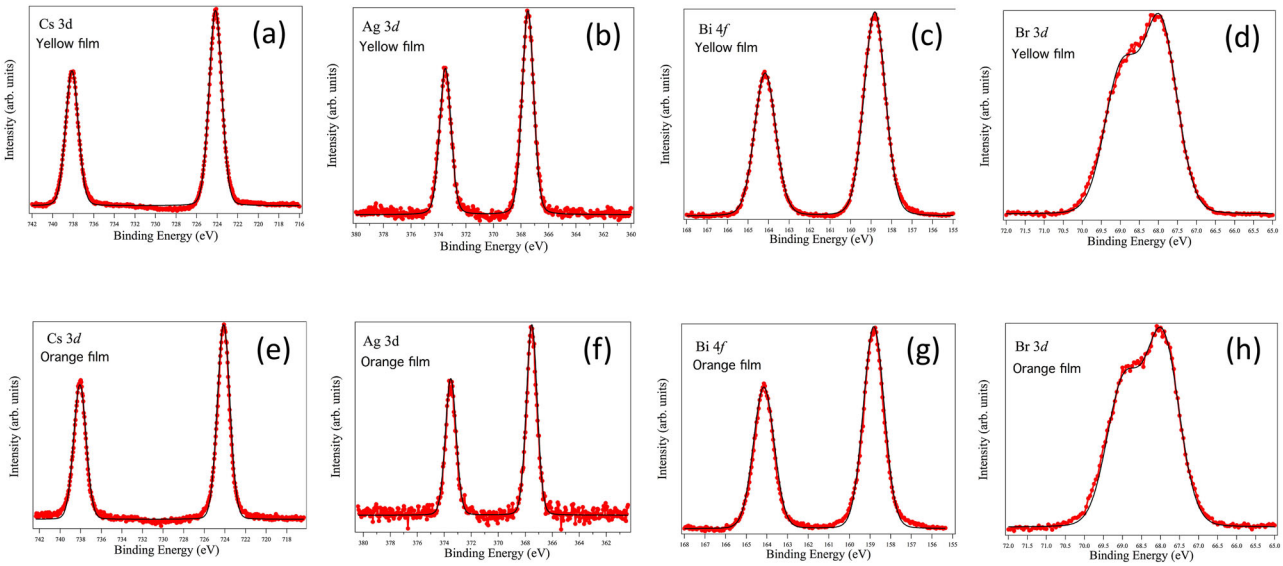


Fig. 6 | C3d, Ag3d, Bi4f, and Br3d core-level spectra and related least-squares fitting. a–d yellow, and **e–h** orange $Cs_2AgBiBr_6$ perovskites. Red dots are the measured spectra, and black lines their least-squares fitting.

perovskite samples, as well as different spectral noise depending on their different scans number.

We describe the process of $Cs_2AgBiBr_3$ perovskite synthesis in H_2O, considering the dissolution chemical reaction of the CsBr, AgBr, and $BiBr_3$ salts in their separate steps.

CsBr is a ionic salt that dissolves in water dissociating into its constituent ions with a physical reaction with it, without chemically react, with a molar solubility product $K_{sp}^{CsBr} = 5.8$ mol/L:

$$CsBr_{solid} + H_2O_{liquid} \rightarrow Cs^+_{aqueous} + Br^-_{aqueous} + H_2O_{liquid}. \quad (1)$$

The molar solubility product of AgBr salt in H_2O is low as approximately $K_{sp}^{AgBr} = 7.31 \times 10^{-7}$ mol/L, where the solid dissolves and dissociates into its constituent Ag^+, Br^- ions, until an equilibrium is reached, without chemical reaction with water:

$$AgBr_{solid} + H_2O_{liquid} \rightleftharpoons Ag^+_{aqueous} + Br^-_{aqueous} + H_2O_{liquid}. \quad (2)$$

Different is the case of $BiBr_3$ salt, which reacts with water, with a process known as hydrolysis, to produce bismuth oxybromide (BiOBr) and soluble hydrobromic acid (HBr):

$$BiBr_{3\,solid} + H_2O_{liquid} \longrightarrow BiOBr_{solid} \downarrow + 2HBr_{aqueous}. \quad (3)$$

The lack of evident XRD peaks of BiOBr in all the XRD spectra of $Cs_2AgBiBr_6$, in general, and in particular in those obtained after immersion in water of the CsBr, AgBr, and $BiBr_3$ salts and of the $Cs_2AgBiBr_6$ powders guarantees the absence of the precipitated BiOBr phase[42] resulting from reaction (3). This implies that the reactions (1), (2), and (3) of the salts with H_2O, separately, are chemically different from the reaction of their combination, which instead leads to the synthesis of the perovskite $Cs_2AgBiBr_6$:

$$2CsBr_{solid} + AgBr_{solid} + BiBr_{3\,solid} + H_2O \longrightarrow Cs_2^{2+}Ag^+Bi^{3+}Br_6^{6-} + H_2O, \quad (4)$$

where water promotes the formation of the perovskite reaction (4), as a catalyst without entering in the final product. This mechanism can be supported considering that the bonds of the $BiBr_3$ salt are not purely covalent, but partially ionic, and in the presence of HBr, the result of reaction (3), would facilitate the presence/formation of both Ag^+Br^- and $Bi^{3+}Br_6^{6-}$ ions despite the low solubility of AgBr.

This proposed mechanism is supported by the electronic properties investigated using X-ray photoemission spectroscopy, on both powders and films of yellow and orange $Cs_2AgBiBr_6$ perovskites. Supplementary Fig. 1 shows a typical photoemission survey, as a function of binding energy (BE), of yellow and orange $Cs_2AgBiBr_6$ perovskite films deposited on ITO and collected with a photon energy of 1486.708 eV of the Al x-ray source.

In addition to the presence of the main peaks of the Cs, Ag, and Bi core levels of the $Cs_2AgBiBr_6$ perovskites, O1s and C1s are marked with two arrows. Taking advantage of these two survey spectra, we can calculate the stoichiometric ratio in the two films, the yellow Supplementary Fig. 1 (a), and the orange Supplementary Fig. 1 (b), by the area under the peaks, after background subtraction. Thus, from the Cs$3d_{5/2}$, Ag$3d_{5/2}$, Bi$4d_{5/2}$, and Br$3d$, core levels, considering the atomic photoionization cross-sections of the various elements, we found a (2:1:1) stoichiometric ratio in both films, in good agreement with the reported XRD results. Except that in the yellow film, there is a small reduction of 15% of intensity of Bi atoms, compared to Ag atoms, still preserving the crystalline structure, but modifying its electronic properties, in agreement with theoretical calculations and experimental measurements[16,19–21,22,37,44].

Figure 6 reports the C$3d$, Ag$3d$, Bi$4f$, and Br$3d$ core-level spectra, red dots, measured from yellow (a–d), and orange (e–h) $Cs_2AgBiBr_6$ perovskites, with hν =1486.708 eV of Al x-ray source. For more quantitative information, after a Shirley background subtraction and least-squares fitting, black lines, using the spin-orbit split Voigt functions, are shown. All core-level spectra exhibit a single component related to the bonds of perovskites. They exhibit no core-level shifts (CLS), ensuring a pure perovskite phase, in close accordance with the XRD spectra.

The Cs$3d$, Ag$3d$, Bi$4f$, and Br$3d$ core-level spectra characteristics, such as BE, Gaussian width, σ_G, and Lorentzian width, Γ_L, the spin-orbit (S.O) splitting, and branching ratio (BR) obtained by the least-squares fitting procedure, are shown in Table 1. The S.O splitting and BRs, for all spectra, are in close agreement with values expected for each atomic level.

It should be noted from the values reported in Table 1 that there is a clear agreement between the reported BEs values for the various core levels in the yellow and orange films, as expected, given the same crystalline structure, but different for the σ_G values, pointing out to a greater disorder in the yellow film. This result is consistent with the presence of defects in the yellow film, which broaden the σ_G, probably caused by a depletion of Bi atoms in the structure.

Figure 7 reports the O$1s$, and C$1s$ core-level spectra, red dots, measured from yellow (a-b), and orange (c-d) $Cs_2AgBiBr_6$ perovskites, also using a

Table 1 | Core-level spectra characteristics from the least-squares fitting procedure

Element	BE (eV)	σ_G (eV)	Γ_L (eV)	SO (eV)	BR
Cs 3d Orange	724.13	0.08	1.40	13.95	1.44
Cs 3d Yellow	724.17	0.14	1.40	13.95	1.44
Ag 3d Orange	367.52	0.08	0.90	6.00	1.39
Ag 3d Yellow	367.50	0.15	0.90	6.00	1.39
Bi 4f Orange	158.82	0.08	1.15	5.33	1.42
Bi 4f Yellow	159.82	0.16	1.15	5.35	1.42
Br 3d Orange	67.95	0.08	1.00	1.03	1.35
Br 3d Yellow	67.95	0.14	1.00	1.03	1.35

BE, S. O, σ_G, Γ_L, and BR parameters are reported.

photon energy of hν =1486.708 eV of Al x-ray source. Also here, after a Shirley background subtraction, the least-squares fitting, black lines, by using the single Voigt functions, are performed. O*1s*, and C*1s* core-level spectra, for both yellow and orange films, exhibit multiple components related to the bonds of perovskites.

As we can clearly observe from Fig. 7, the O1s and C1s spectra for yellow (a, b), and orange (c, d) in $Cs_2AgBiBr_6$ perovskites exhibit multi-components, extrapolated from their least-squares fitting.

The four components of O*1s* are attributed to physisorbed oxygen atoms, oxygen bonded to carbon atoms, and oxygen bonded to tin: $O_{physisorbed}$, O–C, $O–Sn^{4+}$, and $O–Sn^{2+}$, originating from the ITO substrate. Correlatively, the three components present in the core level of C1s are ascribed to carbon atoms bonded to oxygen atoms, to aggregates of carbon atoms with C–O character, C_{sp3}, and C_{sp2}, due to ubiquitous surface impurities when a surface sample is exposed to oxygen and carbon in the air (see Table 2), in good agreement with references[46–48].

It is important to note that there is no presence of hydroxyl groups O–H, (BE = 287.80 eV)[47], completely excluding that the liquid H_2O can remain embedded in the two synthesized perovskites, favouring the escape of water molecules immediately after formation of the $Cs_2AgBiBr_6$ compound, still in liquid phase, and even more during and after their drying (powders and films). No traces of further impurities were revealed by the XPS and PES.

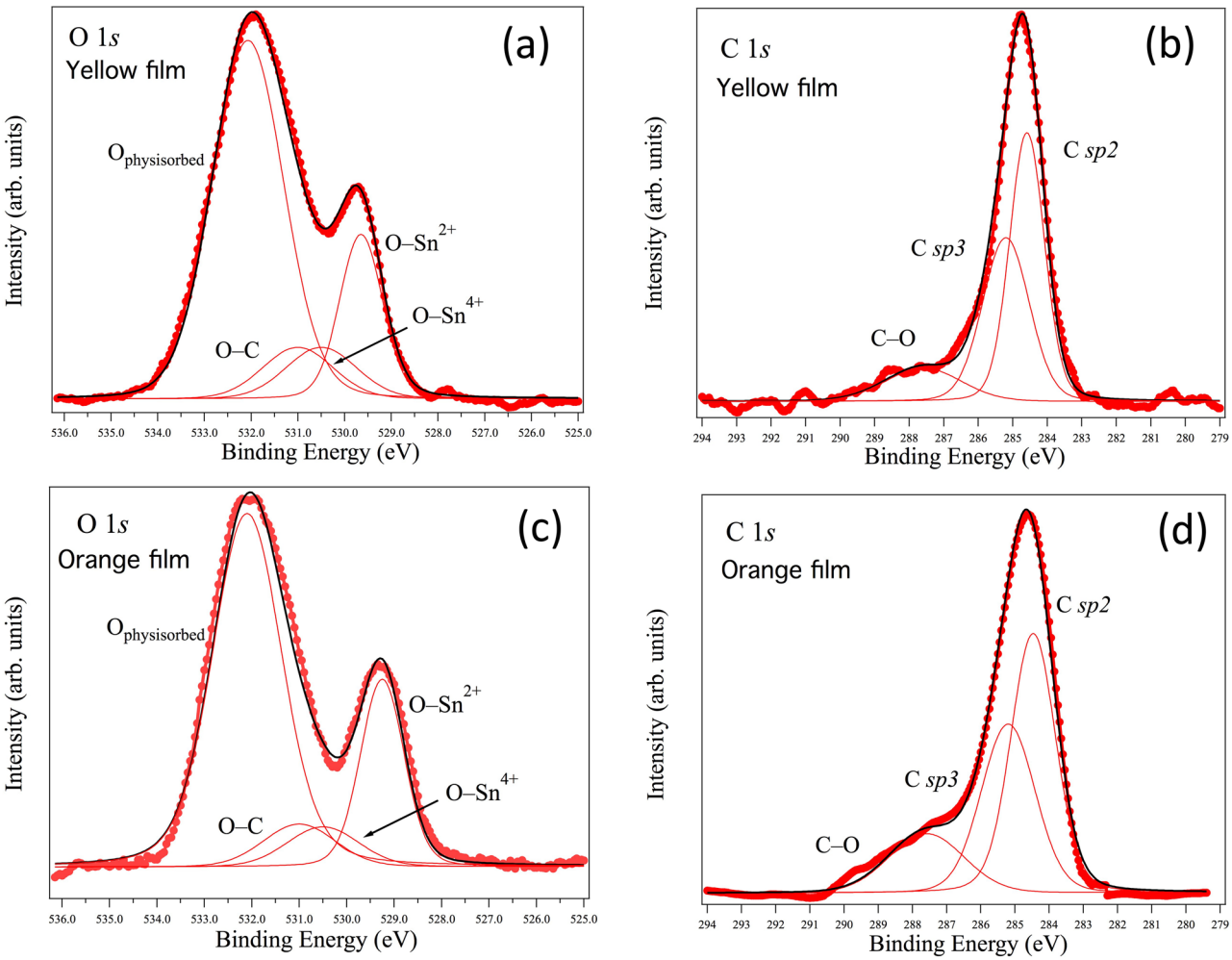


Fig. 7 | O1s and C1s core-level spectra and their least-squares fitting. a, **b** yellow, and **c**, **d** orange $Cs_2AgBiBr_6$ perovskites. Red dots are the measured spectra, and the black lines are their least-squares fitting. Four components: $O_{physisorbed}$, O–C, $O–Sn^{4+}$, and $O–Sn^{2+}$, and three components: C–O, C_{sp3}, and C_{sp2} are present in O*1s* and O*1s* core levels, respectively.

Two photons of 7 keV and 13 keV are selected at the CARNAUBA (SIRIUS) beamline to be more sensitive to the fluorescence emissions of Cs and Ag atoms, and Br, reported in Fig. 8, for yellow and orange films.

Figure 8a, (a') reports the XRF spectra collected on yellow and orange $Cs_2AgBiBr_6$ at a photon energy of 7 keV, and Supplementary Fig. 2a–c, and 2a'-c' their (250 × 250) μm^2 XRF maps. At this excitation energy, the bands in the energy range of (2320-2660) eV, and of (3120–3370) eV, which include the Bi $M_{\alpha1}$ (2422.6 eV) and Ag L_1 (2633.7 eV), and at higher energy the Ag $L_{\beta1}$ (3150.9 eV) and Ag $L_{\beta2,15}$ (3347.8) eV eV) emissions, are clearly visible. The fluorescence in the energy range of (4090–5300) eV, from Cs, involves, instead, the Cs $L_{\alpha2}$ (4272.2 eV), Cs $L_{\alpha1}$ (4280.2 eV), Cs $L_{\beta2}$ (4619.8 eV), Cs $L_{\beta2,15}$ (4935.9 eV), and Cs $L_{\gamma1}$ (5280.4 eV) emissions. The XRF of Br $K_{\alpha2}$ (11877.6), $K_{\beta1}$ (13291.4), $K_{\beta3}$(12934.8), and Bi $L_{\alpha1}$ (10838.8), and $L_{\alpha2}$ (10730.93 eV) are reported in (b), (b'), for yellow and orange films, respectively, while Supplementary Fig. 2d, e, and 2d', e' their (250 × 250) μm^2 XRF maps.

Table 2 | O1s and C1s core-level spectra characteristics from the least-squares fitting procedure

Element	Component	BE (eV)	σ_G (eV)	Γ_L (eV)
O 1 s Yellow	$O_{physisorbed}$	532.05	0.40	1.50
	O–C	531.00	0.14	1.70
	O–Sn^{4+}	530.40	0.13	1.70
	O–Sn^{2+}	529.65	0.14	1.00
C 1 s Yellow	O–C	287.59	0.15	2.50
	C_{sp3}	285.20	0.16	1.50
	C_{sp2}	284.59	0.15	1.10
O 1 s Orange	$O_{physisorbed}$	532.10	0.40	1.50
	O–C	531.00	0.14	1.70
	O–Sn^{4+}	530.50	0.13	1.70
	O–Sn^{2+}	529.25	0.14	1.00
C 1 s Orange	O–C	287.59	0.15	2.50
	C_{sp3}	285.20	0.19	1.80
	C_{sp2}	284.47	0.25	1.40

. BE, S. O, σ_G, and Γ_L parameters for yellow and orange films are reported.

As we can observe, both films have the same XRD spectroscopic features for Cs, Ag, Bi, and Br, highlighting, in agreement with the core levels photoemission spectroscopy, a similar atomic composition in yellow and orange $Cs_2AgBiBr_6$ perovskites. All reported XRF maps show the grainy nature of the two films.

This was further confirmed by a pivotal *in-operando* experiment performed on a freshly prepared wet orange film sample, and on the same one after applying a temperature ramp up to T = 110 °C, and waiting for it to dry (see Fig. 9). The related XRF maps are shown in Supplementary Fig. 3.

Even in this case, all spectroscopic characteristics for Cs, Ag, Bi, and Br remain unchanged, confirming the absence of water in the synthesized perovskites, due to the fact that the H_2O molecule allows their formation, not participating in the reaction, but just evaporating.

It is well established that both experimentally and theoretically the perovskite $Cs_2AgBiBr_6$ is a semiconductor having energy bands exhibiting an indirect gap[9,10,12,16,21,43], whose value of 1.95 eV, including an assisting phonon energy of 0.12 eV, was experimentally evaluated[12], through the optical properties, showing an absorption region starting at about 1.8 eV with a rapid increase to 2.1 eV[12].

The mouldability of the crystalline structure of the $Cs_2AgBiBr_6$ perovskite makes it extremely interesting since the electronic properties can be easily modified, increasing or reducing the intrinsic gap of the material[9,10,16,43]. Thus, the energy gap can be reduced by a few tenths of eV, leading to a lowest band gap of 1.72 eV, by varying the degrees of Ag–Bi

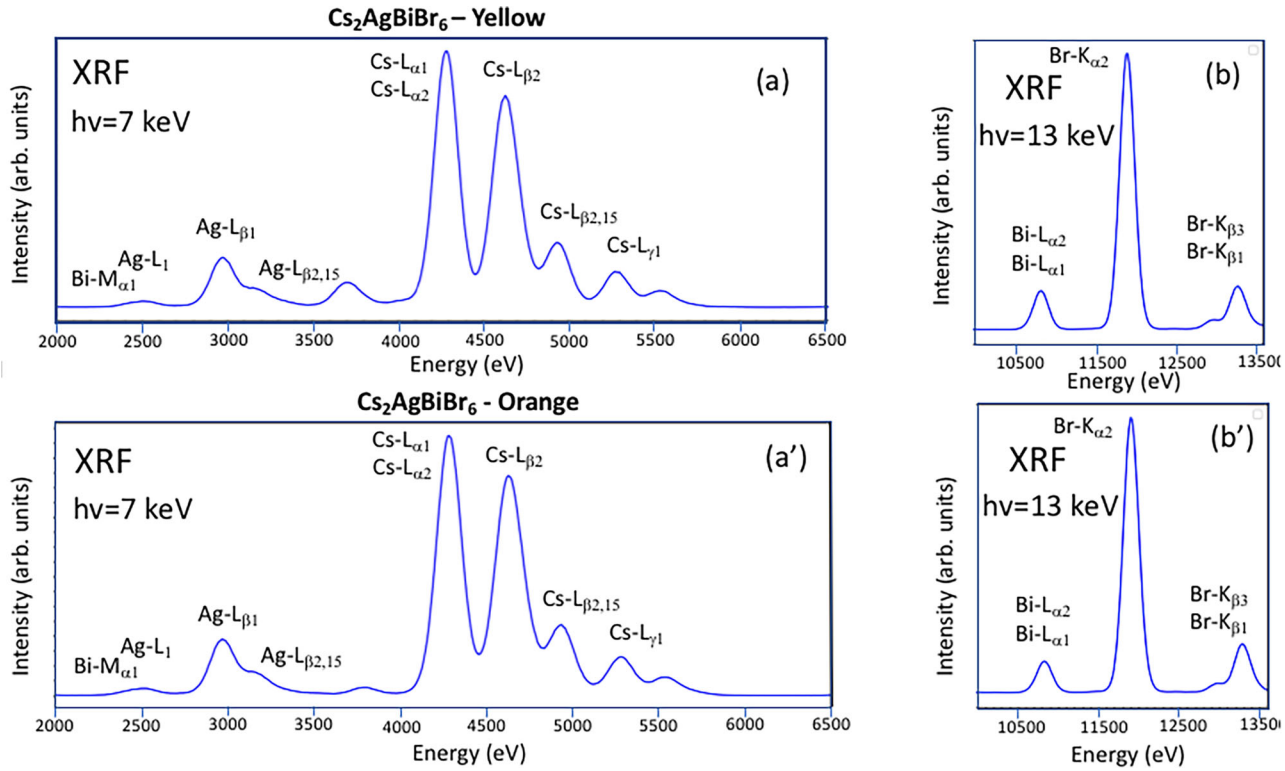


Fig. 8 | X-ray fluorescence spectroscopy from yellow films at RT. a (a') and **b** (b') XRF spectra at hν = 7 keV and 13 keV, respectively, on yellow and orange films.

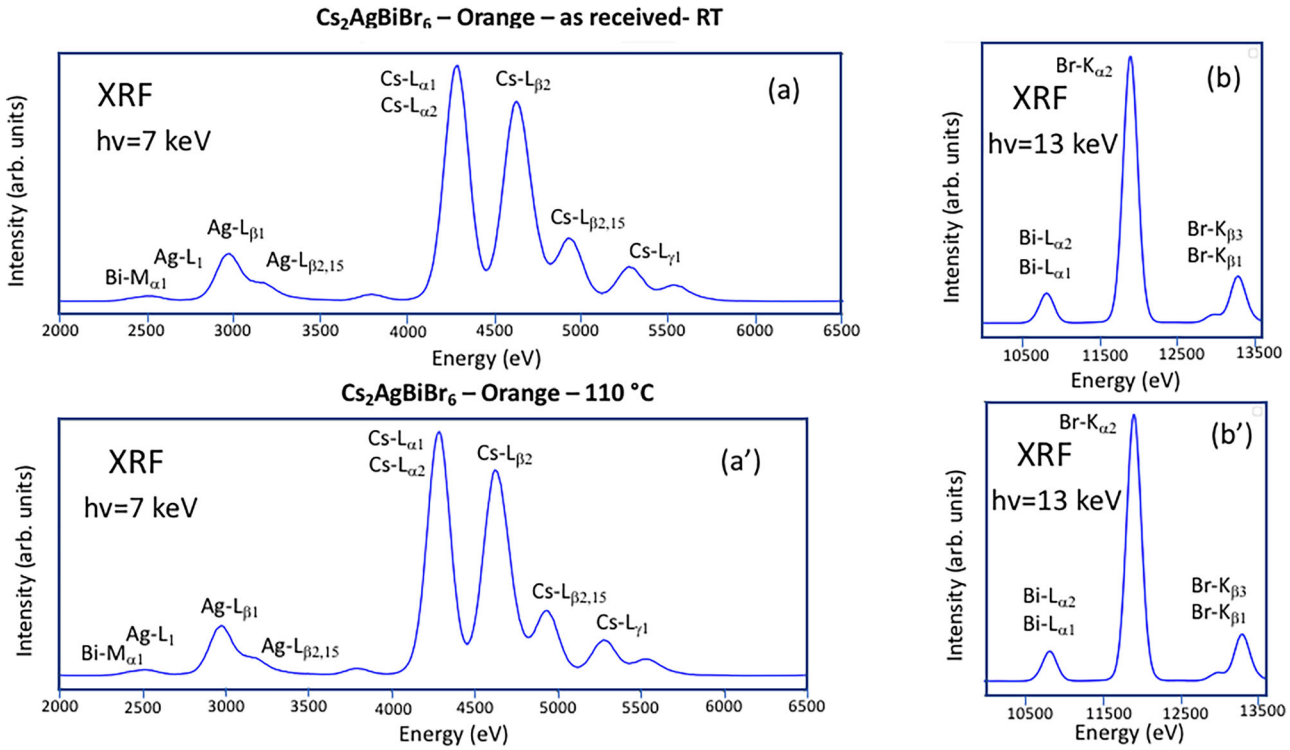


Fig. 9 | X-ray fluorescence spectroscopy from in-operando orange films at RT and T = 110 °C. a (a'), **b** (b') XRF spectra at hν = 7 keV, and 13 keV, respectively, on in-operando orange films at RT (wetting film), and at T = 110 °C (dried film).

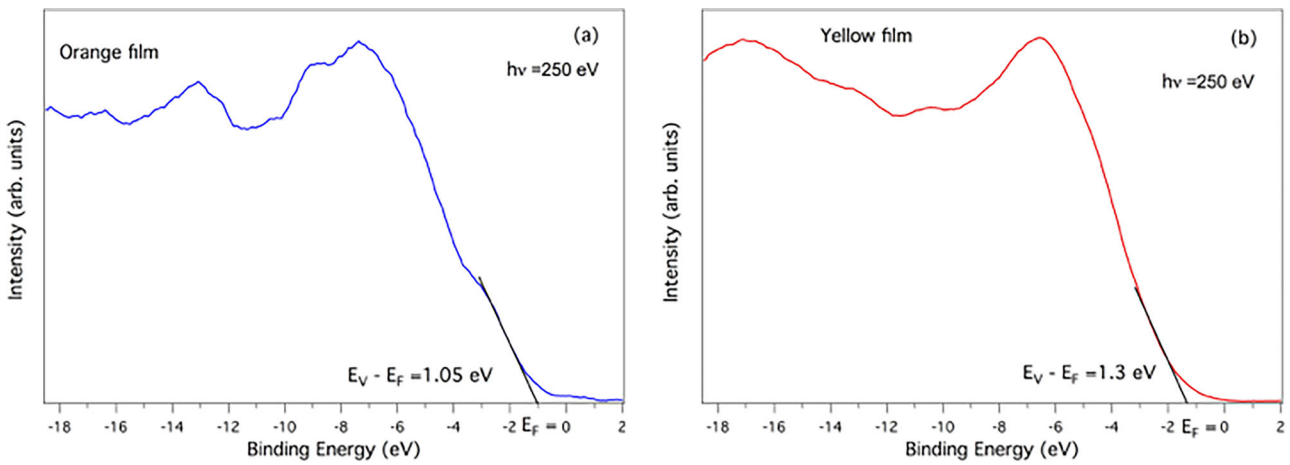


Fig. 10 | Valence bands from yellow and orange $Cs_2AgBiBr_6$ perovskites. a Valence band edge near the Fermi level set to zero E_V-E_F = 1.05 eV, orange, and **b** E_V-E_F = 1.30 eV for yellow films, respectively.

atomic order/disorder in the crystal structure, constituting a valuable source of gap state defects[16].

Similarly, it is possible to switch from orange $Cs_2AgBiBr_6$ perovskite to dark red or light yellow by inserting, in place of the Bi atoms, doping, antimony, or In atoms, which modify the indirect gap as small as 1.82 eV, and as large as 2.27 eV, respectively[21].

A novel fully reversible effect, called thermochromism, has recently been observed in both single crystals and films of $Cs_2AgBiBr_6$ perovskite[22]. Variable temperature XRD/Raman spectroscopy measurements indicated a variation/fluctuation in the length of Ag–Br and Bi–Br bonds at different applied temperatures, as confirmed by first-principle molecular dynamics simulations, including the spin–orbit coupling effect, and strong electron–phonon coupling[22].

To modulate the properties of the double $Cs_2AgBiBr_6$ perovskite, in our case we adopted the strategy of using the "sub-stoichiometry" (1:1:1) ratio of the precursor salts to synthesize a yellow $Cs_2AgBiBr_6$ perovskite, obtaining a formula of the type $Cs_2(Ag_xBi_{1-x})Br_6$, where there is an imbalance between Ag and Bi atoms in the perovskite structure, to realize a crystal-engineering having directly different optic/electronic properties.

Figure 10 reports the valence bands (VB) acquired in integrated mode at the IPE beamline (SIRIUS) with synchrotron radiation, using a photon hν = 250 eV, from yellow and orange $Cs_2AgBiBr_6$ perovskites to get information on the total density of states (DOS) near the Fermi level, conventionally set to zero.

Although the total DOS structures in the two films are similar and attributed by first-principles calculations to mainly originate from

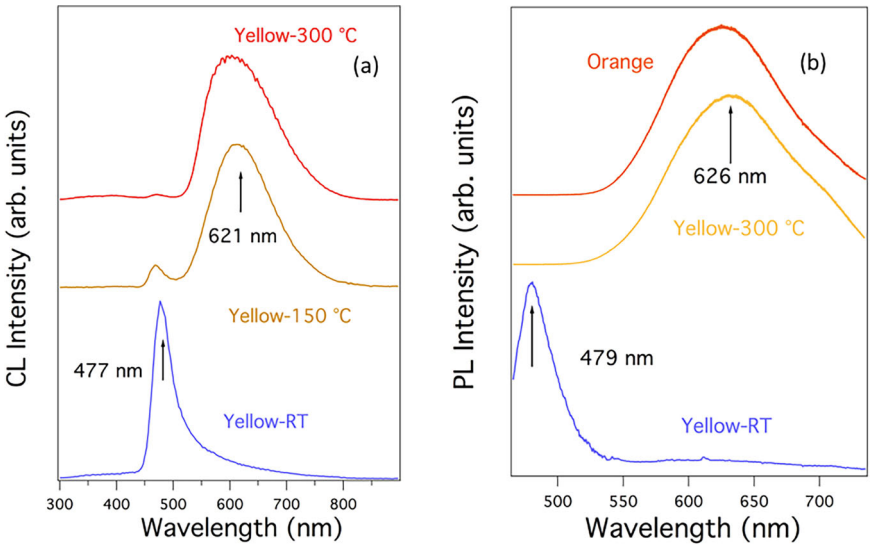


Fig. 11 | Cathodoluminescence and photoluminescence spectra of yellow-orange $Cs_2AgBiBr_6$ films. a CL of yellow film at RT and after annealing at 150 °C and 300 °C, **b** PL of yellow film at RT and after annealing at 300 °C, and orange film.

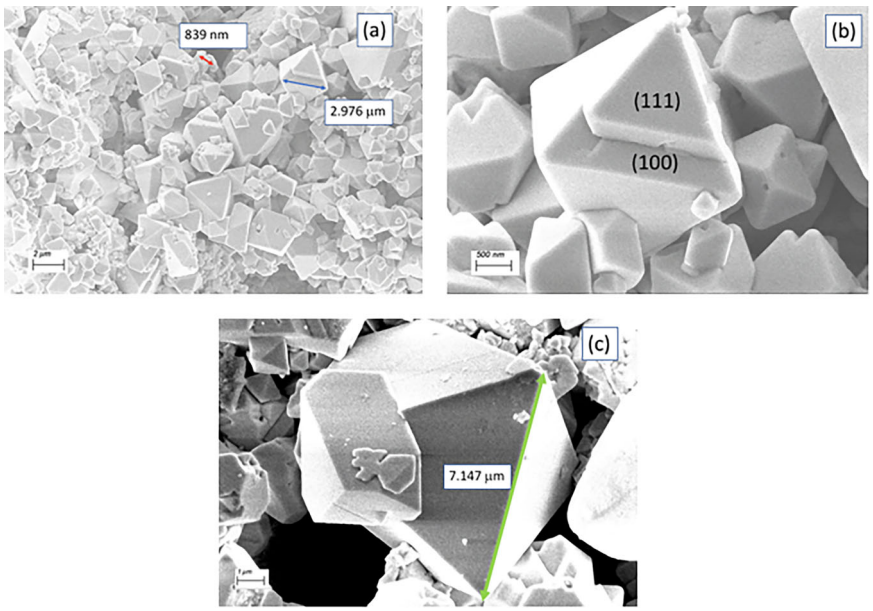


Fig. 12 | SEM images of orange $Cs_2AgBiBr_6$ at different magnifications. a at 4.25 k×, **b** at 18.46 k×, and **c** at 8.85 k×, with an electron energy beam of $E_p = 5$ keV.

hybridized Ag-d/Br-*p* states, and Bi-*s* character mixed at the band edge[16], they exhibit different electronic contributions close to the Fermi level.

This can be obtained by linearly extrapolating the top of the VBs of the two films. Our yellow and orange $Cs_2AgBiBr_6$ perovskites show two slightly different energy gaps, aiming for the distance between the top of the VB and Fermi level, E_V-E_F = 1.05 eV, half of gap energy, considered symmetric, thus, giving a gap = 2.10 eV, in the case of the orange film, and E_V-E_F = 1.3 eV, a gap = 2.60 eV, for the yellow one, in good agreement with what reported in refs. 21,22, and significantly in line with their chromatism[22].

To further characterize the electronic and optical properties of the yellow and orange $Cs_2AgBiBr_6$ perovskite films, we performed transmittance and reflectance measurements from which the absorption is obtained, as well as photoluminescence and cathodoluminescence measurements. Supplementary Fig. 4 reports the optical properties, through the measurement of the transmittance and reflectance, of the orange perovskite film $Cs_2AgBiBr_6$ performed using a UV-VIS lamp, with a wavelength range from 800 nm to 250 nm, while Supplementary Fig. 5 those of yellow perovskite film $Cs_2AgBiBr_6$, evidencing different cut-off edge in line with their different energy band gaps.

What can be noted is that, as previously discussed, with the same crystalline structure, cubic *Fm-3m*, this $Cs_2AgBiBr_6$ perovskite can present different optical and electronic properties depending on the treatments applied to it. This is clear from the cathodouminescence spectra, reported in Fig. 11a, where the yellow spectra at RT, 150 °C and 300 °C, are compared.

Here, are also shown broad spectra of the order of about a hundred nm for the two CL curves recorded from perovskite samples after the annealing at 150 °C and 300 °C. They are peaked at about 621 nm, with a small peak at 477 nm at higher energy, residue of the yellow perovskite, and strongly present on the yellow sample performed at RT, in line with all previous literature[10,12,16,20–23,38,39,42].

As we can see the PL spectra reported in Fig. 11b are in good agreement with results of cathodoluminescence, with peak located at 479 nm and 626 nm for yellow, yellow-300 °C, and orange films.

Figure 12 shows the morphological properties of the orange $Cs_2AgBiBr_6$ perovskite film imaged at different magnifications, 4.25 k×, 18.46 k×, and 8.85 k× (c), with an electron beam energy of 5 keV.

It is clearly evident that there are perovskite crystals, with structures that have dimensions ranging from hundreds of nm to a few/several microns, as marked by the blue and red arrows in Fig. 12a, just to highlight a

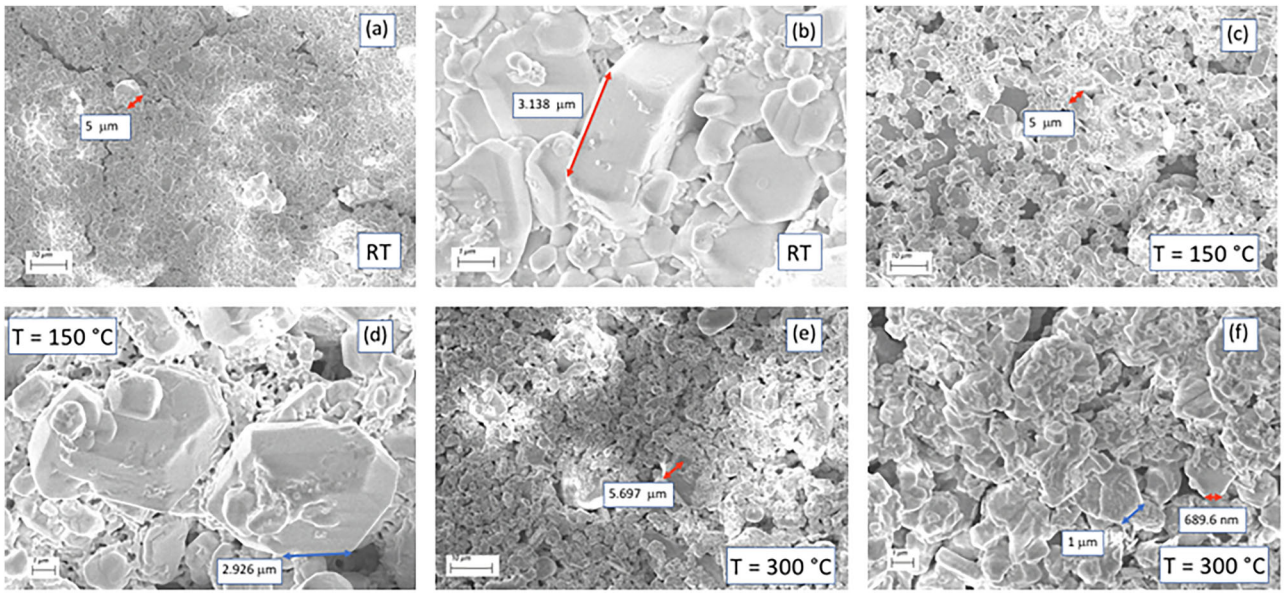


Fig. 13 | SEM images of the yellow-orange $Cs_2AgBiBr_6$ film with different magnifications. a at RT (1.02 k×) and **b** (10.03 k×); **c** post annealing at 150 °C (1.06 k×) and **d** (6.03 k×); **e** 300 °C (1.25 k×), and **f** (6.80 k×), at Ep = 5KeV.

couple of them, as well as in Fig. 12c, where a side of 7.147 µm, green arrow, was found.

In Fig. 12b, the magnification of the crystal, marked with blue arrow in (a), is reported to better focus on the tetrahedral shape of the micro-nano crystals of $Cs_2AgBiBr_6$ perovskite, which are the signature of the cubic crystalline phase of this compound. Interestingly, the crystals are ordered, in the structure, often presenting sides of the double pyramid, showing the same size, and extremely (111) and (100) ordered planes, in perfect agreement with the XRD measurements reported above.

Figure 13, instead, shows the morphological properties of yellow $Cs_2AgBiBr_6$ perovskite films imaged at different magnifications, and post annealing temperatures: at RT (a) (1.02 k×) and (b) (10.03 k×); post annealing at 150 °C (c) (1.06 k×) and (d) (6.03 kx); and 300 °C (e) (1.25 k×) and (f) (6.80 k×), at Ep= 5KeV.

Comparing the SEM images collected on the yellow films in Fig. 13, it can be seen that, in general, the morphological texture, which also reports the presence of crystallites, is much more compact than the films of orange $Cs_2AgBiBr_6$ perovskite. At room temperature, structures of a few microns can be observed, as marked by the double red arrows in (a) and (b), with about 3 and 5 µm.

The application of post annealing at T = 150 °C and 300 °C seems to make the morphology of the films a little more jagged, as highlighted in images (c) and (d), at 150 °C, and (e) and (f) at 300 °C, where the presence of more disconnections between the crystallites can be observed.

We worth noting that all measurements reported have been done on all prepared samples, some of those even prepared two years earlier, and all structural, optical, and electronic properties remained unchanged. In general, it can be stated that the orange and yellow films of the perovskite $Cs_2AgBiBr_6$, synthesized by hydro solution, are very easy to handle and, having different optical and electronic properties and with the same crystalline structure, promise the feasibility of a wide range optoelectronic devices.

Finally, the *perovskites water-synthesis* process, reported in this paper, nicely evokes that almost two centuries ago, in 1839, the German mineralogist, Gustavus Rose[49], defined the properties and chemical composition of a natural mineral, found in the Ural Mountains of Russia, the $CaTiO_3$, new to science until then and totally formed in nature.

He namead the $CaTiO_3$, mineral, in honour to the Russian mineralogist Lev Alekseevič Perovskij, perovskite[49,50]. More than a century later, in 1945, Helen Dick Megaw[51], revealed the crystal structure of the barium titanate ($BaTiO_3$) mineral, known belonging to the same group of compounds, and having the structure of perovskite type, such as the $CaTiO_3$[49].

Most likely, in nature, the water has been playing a fundamental role in inorganic compound formation, similar to our water-synthesis process of $Cs_2AgBiBr_6$ perovskite.

Methods

The powder and films of perovskite $Cs_2AgBiBr_6$ were synthesized at the IC11 Laboratory at CNR-ISM, (Roma, Italy), by liquid phase deposition. The method uses AgBr (99.999 %), $BiBr_3$ (99.999 %), and CsBr (99.999 %) precursor salts, purchased by Alfa Aesar (AgBr, $BiBr_3$) and TCI (CsBr), respectively, without any further purification. They have been appropriately manual mixed, light pounding with a pastel, and/or just weigh, with no further mixing, in air in suitable concentrations, to achieve the stoichiometry and sub-stoichiometry $Cs_2AgBiBr_6$ perovskite powders. Different concentrations of, CsBr, AgBr, and $BiBr_3$ salts produces $Cs_2AgBiBr_6$ perovskite colour orange (2:1:1), stoichiometric, and yellow (1:1:1), sub-stoichiometric, in molar weights. After $Cs_2AgBiBr_6$ perovskite powders formation, in different colours, they were dissolved in bi-distilled and deionized water, by a system composed of two purifiers (Elix, Merk) and Milli-Q (Merk), producing, a high resistance of (14–18) M ohm, and dropped/spread on indium tin oxide/glass substrates. The yellow and orange $Cs_2AgBiBr_6$ perovskites were allowed to dry in air, producing compact films. The yellow films were, further, annealed at temperatures of 150 °C and 300 °C. All samples have been prepared in a typical indoor atmospheric conditions (T = 25 °C, humidity, 40–60%).

All X-ray diffraction measurements were performed at Gifu University (Gifu, Japan), except the XRD pattern of Fig. 5, which were performed at Roma II University, Dep. of Engineering (Roma, Italy), by means of a Rigaku SmartLab diffractometer, working in (ϑ–2ϑ) Bragg–Brentano geometry, equipped with a Cu source ($K_{\alpha 1}$ = 1,54060 Å) and a D/teX Ultra 250 silicon strips detector. XRD spectra (5°–50°) were acquired in a single/double scan with a step of 0.05 °, with ~ 0.2 s/pt, and a horizontal slit of 2/5 mm. The sample morphology was investigated by scanning electron microscopy measurements performed using a ZEISS SIGMA 300 FESEM microscope, while the UV-VIS (SHIMADZU UV-2700/MPC-2700) apparatus was used to study the materials optical properties by means of transmittance and reflectance measurements, at CNR-ISM (Rome-Itly). Spectrally resolved cathodouminescence measurements of the samples were recorded at the Semiconductor Physics and

Technology Laboratory, Department of Innovation Engineering of University of Salento (Lecce, Italy), using a field-emission scanning electron microscope (FESEM) model Zeiss Sigma VP equipped with a Gemini I electron column and a Gatan MonoCL4 system at RT, and with an acceleration voltage of 20 kV. Photoluminescence measurements were performed at CNR-ISM (Roma, Italy), by means of inVia Renishaw MicroRaman system with wavelength of 457 nm, × 5 objective and laser power of 0.5 %, at RT.

Nano-XRF mapping of the perovskites were obtained at the CARNAUBA beamline[52] of the Brazilian Synchrotron Light Laboratory (LNLS) part of the Brazilian Center for Research Energy and Materials (CNPEM). An X-ray beam of 300×300 nm scanned the sample in fly scan mode. Two energies of excitation were used to optimize the XRF emission, 7 and 13 keV. The maps were obtained in a field of view of (250 × 250) μm2.

In-operando spectra were acquired at room temperature and by ramping the temperature up to 110 °C, by preparing the orange $Cs_2AgBiBr_6$ perovskites in-situ, adding water to already synthesised perovskite powders. The heating of the sample was performed in-situ using the photovoltaic holder of the beamline. All the measurements were performed in air.

Valence band photoemission was taken at IPE beamline, of the Brazilian Synchrotron Light Laboratory (LNLS), by a photon energy of 250 eV, with a resolution of 0.10 eV (LNLS).

Photoemission survey and core-level X-ray photoelectron spectroscopy (XPS) was performed at Nagoya University (Japan) using an ESCALAB 250Xi (Thermo Scientific). The excitation source of 1486.6 eV from a $K_{\alpha 1}$ Al X-ray source was used with a resolution less than 0.45 eV.

Conclusions

The synthesis and study of the orange and yellow double cation lead-free perovskite $Cs_2AgBiBr_6$, both in powder and in film form, have been achieved, using an innovative procedure completely free of chemical solvents. Using different ratios between the molar weights of the precursor salts of CsBr, AgBr, and $BiBr_3$, it is possible to switch from orange to yellow perovskite. The methodology involves the use of mixing, and no-mixing, among the salts precursor powders and a liquid bath of water.

The structural, morphological, optical and electronic properties of $Cs_2AgBiBr_6$ lead-free perovskite films and powders, were exploited, by several techniques, such as x-ray diffraction, scanning electron microscopy, photoluminescence, cathodoluminescence, and transmittance, reflectance, absorption optical measurements, synchrotron radiation valence band photoemission, and x-ray fluorescence spectra and maps, as well as x-ray core levels photoemission spectroscopies. XRF measurements were also collected on just synthesised orange $Cs_2AgBiBr_6$ perovskite *in-operando* on-chip at RT and at temperature of 110 °C.

Cubic phase, *Fm-3m* group, with a gap of about 2.10 to 2.6 eV, as deduced by valence band spectroscopy, and confirmed from the optical properties and photo-cathode luminescence measurements was found. Indeed, from three-dimensional tetrahedral nanocrystals to more flat structures, displaying different sizes, from hundreds of nm to several microns, were observed by SEM, confirming the cubic structure found in the XRD patterns. Core levels fitting procedure and synchrotron radiation x-ray fluorescence spectroscopies give information on the formation of $Cs_2AgBiBr_6$ perovskite, during the in solution water-process.

Remarkably, the synthesis of perovskite free of lead and chemical solvents and therefore totally "green", is a significant step forward in the development and research of extremely useful materials for wide gap optoelectronic devices, and/or as photosensitive material for solar cells, in promising tandem technology nowadays, by using a common nontoxic liquid, i. e. the water.

Indeed, three-dimensional tetrahedral nanocrystals from hundreds of nanometres to micrometres in of size, observed by SEM, confirming the cubic structure found in the XRD patterns, conferring to this water-perovskite synthesis a novelty, inside the perovskites realm.

Data availability

All data are available in the main text and supplementary information file.

Received: 4 August 2025; Accepted: 24 June 2026;
Published online: 20 August 2026

References

1. Kronawitter, S.M. & Kieslich, G. The wondrous world of ABX_3 molecular perovskites. *Chem. Commun.* **60**, 11673 (2024).
2. Roy, P. et al. Perovskite solar cells: a review of the recent advances. *Coatings* **12**, 1089 (2022).
3. Anaya, M., Lozano, G., Calvo, M.E. & Míguez, H. ABX_3 Perovskites for tandem solar cells. *Joule* **1**, 769 (2017).
4. Shi, D. et al. Low trap-state density and long carrier diffusion in organolead trihalide perovskite single crystals. *Science* **347**, 519 (2015).
5. Kojima, A. et al. Organometal halide perovskites as visible-light sensitizers for photovoltaic cells. *J. Am. Chem. Soc.* **131**, 6050 (2009).
6. NREL. Best Research-Cell Efficiency Chart, (2/2026), https://www.nrel.gov/pv/cell-efficiency.html.
7. Babayigit, A. et al. Toxicity of organometal halide perovskite solar cells. *Nat. Mat.* **15**, 247 (2016).
8. Katelyn, P. G. et al. Sustainability in perovskite solar cells. *ACS Appl. Mater. Interfaces* **13,** (2021)
9. Filip, M. R. et al. Band gaps of the lead-free halide double perovskites $Cs_2BiAgCl_6$ and $Cs_2BiAgBr_6$ from theory and experiment. *J. Phys. Chem. Lett.* **7**, 2579 (2016).
10. Volonakis, G. et al. $Cs_2InAgCl_6$: a new lead-free halide double perovskite with direct band gap. *J. Phys. Chem. Lett.* **8**, 772 (2017).
11. Volonakis, G. et al. Lead-free halide double perovskites via heterovalent substitution of noble matals. *J. Phys. Chem. Lett.* **7**, 1254 (2016).
12. Slavney, A. H. et al. A Bismuth-Halide double perovskite with long carrier recombination lifetime for photovoltaic applications. *J. Am. Chem. Soc.* **138**, 2138 (2016).
13. Ning, W. & Gao, F. Structural and functional diversity in lead-free halide perovskite materials. *Adv. Mater.* **31**, 1900326 (2019).
14. Zhou, H. et al. Interface engineering of highly efficient perovskite solar cells. *Science* **345**, 542 (2014).
15. deQuilettes, D. W. et al. D. S. Impact of microstructure on local carrier lifetime in perovskite solar cells. *Science* **348**, 683 (2015).
16. Ji, F. et al. Lead-free halide double perovskite $Cs_2AgBiBr_6$ with decreased band gap. *Angew. Chem., Int. Ed.* **59**, 15191 (2020).
17. Schade, L. et al. Structural and optical properties of $Cs_2AgBiBr_6$ double perovskite. *ACS Energy Lett.* **4**, 299 (2019).
18. Fu, R. et al. Pressure-induced structural transition and band gap evolution of double perovskite $Cs_2AgBiBr_6$ nanocrystals. *Nanoscale* **11**, 17004 (2019).
19. Li, Q. et al. High-Pressure band-gap engineering in lead-free $Cs_2AgBiBr_6$ double perovskite. *Angew. Chem. Int. Ed.* **56**, 15969 (2017).
20. Slavney, A.H. et al. Defect-induced band-edge reconstruction of a bismuth-halide, double perovskite for visible-light absorption. *J. Am. Chem. Soc.* **139**, 5915 (2017).
21. Du, K. et al. Bandgap engineering of lead-free double perovskite $Cs_2AgBiBr_6$ through trivalent metal alloying. *Angew. Chem., Int. Ed.* **56**, 8158 (2017).
22. Ning, W. et al. Thermochromic lead-free halide double perovskites. *Adv. Funct. Mater.* **29**, 1807375 (2019).
23. Greul, E. et al. Highly stable, phase pure $Cs_2AgBiBr_6$ double perovskite thin films for optoelectronic Applications. *J. Mater. Chem. A* **5**, 19972 (2017).
24. Pan, W. et al. $Cs_2AgBiBr_6$ single-crystal X-ray detectors with a low detection limit. *Nat. Photonics* **11**, 726 (2017).

25. Lei, L.-Z. et al. High-efficiency and air-stable photodetectors based on lead-free double perovskite $Cs_2AgBiBr_6$ thin films. *J. Mater. Chem. C.* **6**, 7982 (2018).
26. Lei, H., Hardy, D. & Gao, F. Lead-free double perovskite $Cs_2AgBiBr_6$: fundamentals, applications, and perspectives. *Adv. Funct. Mater.* **31**, 2105898–29 (2021).
27. Chu, L. et al. Lead-free halide double perovskite materials: a new superstar toward green and stable optoelectronic applications. *Nano-Micro Lett.* **11**, 16 (2019).
28. Ravi, V. K. et al. Initiation and future prospects of colloidal metal halide double-perovskite nanocrystals: $Cs_2AgBiBr_6$ (X = Cl, Br, I). *J. Mater. Chem. A* **6**, 21666 (2018).
29. Yang, X. et al. Simultaneous power conversion efficiency and stability enhancement of $Cs_2AgBiBr_6$ lead-free inorganic perovskite solar cell through adopting a multifunctional dye interlayer. *Adv. Funct. Mater.* **30**, 2001557 (2020).
30. Shockley, W. et al. Detailed balance limit of efficiency of p-n Junction solar cells. *J. Appl. Phys.* **32**, 510–519 (1961).
31. Kirchartz, T. & Rau, U. What makes a good solar cell? *Adv. Energy Mater.* **8**, 1703385 (2018).
32. Ning, W. et al. Long electron–hole diffusion length in high-quality lead-free double perovskite films. *Adv. Mater.* **30**, 1706246 (2018).
33. Wang, B. et al. Photoactive Zn-chlorophyll hole transporter-sensitized lead-free $Cs_2AgBiBr_6$ perovskite solar cells. *Sol. RRL* **4**, 2000166 (2020).
34. Wang, B. et al. Chlorophyll derivative-sensitized TiO_2 electron transport layer for record efficiency of $Cs_2AgBiBr_6$ double perovskite solar cells. *J. Am. Chem. Soc.* **143**, 2207–2211 (2021).
35. Yang, X. Recent advances in $Cs_2AgBiBr_6$-based halide double perovskites as lead-free and inorganic light absorbers for perovskite solar cells. *Energy Fuels* **34**, 10513 (2020).
36. Sheng, R. et al. Four-terminal tandem solar cells using $CH_3NH_3PbBr_3$ by spectrum splitting. *J. Phys. Chem. Lett.* **6**, 3931 (2015).
37. Ji, F. et al. Near-infrared light-responsive Cu-doped $Cs_2AgBiBr_6$. *Adv. Funct. Mater.* **30**, 2005521 (2020).
38. Zelewski, S. J. et al. Revealing the nature of photoluminescence emission in the metal-halide double perovskite $Cs_2AgBiBr_6$. *J. Mater. Chem. C.* **7**, 8350 (2019).
39. Creutz, S.E. et al. Colloidal nanocrystals of lead-free double-perovskite (elpasolite) semiconductors: synthesis and anion exchange to access new materials. *Nano Lett.* **18**, 1118 (2018).
40. Bekenstein, Y. et al. The making and breaking of lead-free double perovskite nanocrystals of Cesium Silver−Bismuth halide compositions. *Nano Lett.* **18**, 3502–3508 (2018).
41. Daem, N. et al. Spray-coated lead-free $Cs_2AgBiBr_6$ double perovskite solar cells with high open-circuit voltage. *Sol. RRL* **5**, 2100422 (2021).
42. Fan, P. et al. Single-source vapor-deposited $Cs_2AgBiBr_6$ thin films for lead-free perovskite solar cells. *Nanomaterials* **9**, 1760–13 (2019).
43. McClure, E. T., Ball, M. R., Windl, W. & Woodward, P. M. $Cs_2AgBiBr_6$ (X = Br, Cl): new visible light absorbing, lead-free halide perovskite semiconductors. *Chem. Mater.* **28**, 1348 (2016).
44. Yuan, W. et al. In situ regulating the order–disorder phase transition in $Cs_2AgBiBr_6$ single crystal toward the application in an X-ray detector. *Adv. Funct. Mater.* **29**, 1900234 (2019).
45. De Padova, P. et al. The role of SiO_2 buffer layer in the molecular beam epitaxy growth of $CsPbBr_3$ perovskite on Si(111). *Sci. Rep.* **14**, 23618 (2024).
46. Dey, R. M., Pandey†, M., Bhattacharryya, D., Patil, D. S. & Kulkarini, S. K. Diamond like carbon coatings deposited by microwave plasma CVD: XPS and ellipsometric studies. *Bull. Mater. Sci.* **30**, 541 (2007).
47. Huang, J. et al. Construction of PDIsa/BiOBr type-I scheme heterojunction for efficient ciprofloxacin photocatalytic degradation. *Environ. Sci. Pollut. Res.* **30**, 19210 (2023).
48. Kwoka, M. et al. XPS study of the surface chemistry of L-CVD SnO_2 thin films after oxidation. *Thin Solid Films* **490**, 36 (2005).
49. Rose, G. Beschreibung einiger neuen Mineralien des Urals. *Poggendorffs Ann. Phys. Chem.* **124**, 551 (1839).
50. Katz, E. A. Perovskite: Name Puzzle and German-Russian Odyssey of Discovery. *Helv. Chim. Acta*, **103**, https://doi.org/10.1002/hlca.202000061 (2020).
51. Megaw, H. Crystal structure of barium titanate. *Nature.* **155**, 484 (1945).
52. Lena, F. R. et al. A novel sample holder for operando X-ray nanoscopy of perovskite solar cells, euspen's 23rd International Conference & Exhibition, Copenhagen, DK, June 2023, www.euspen.eu.

Acknowledgements

This work was supported by the project "*Progetti di Ricerca@CNR Bando 2020*", "*High Efficiency Lead-Free Perovskite Solar Cells for Indoor-Outdoor Applications*" (HELFO) project, and CNR-Short Term Mobility, 2024 (Paola De Padova). A.D.C. acknowledges the support from the Horizon Europe Framework Programme (HORIZON) research and innovation Programme under the grant agreement No 101122327 (SMARTLINE-PV). We warmly appreciate the invaluable technical support provided by Luca Imperatori, Marco Guaragno, and Sandro Priori. This research used facilities of the Brazilian Synchrotron Ligh.t Laboratory (LNLS), part of the Brazilian Center for Research in Energy and Materials (CNPEM), a private non-profit organization under the supervision of the Brazilian Ministry for Science, Technology, and Innovations (MCTI). The [CARNAUBA/IPE] beamline staff is acknowledged for the assistance during the experiments [Proposal ID, CARNAUBA: 20241712; Proposal ID, IPE: 20241719].

Author contributions

P. D. P. conceived the idea of this project. P. D. P. and B. O. grown/synthesised the powder and $Cs_2AgBrBr_6$ films. P. D. P. and O. K., performed the XRD measurements and relative data analysis; P. D. P. performed SEM/Optical measurements and relative data analysis, P. D. P., F. R., performed PL of Fig. 11b, and XRD of Fig. 5A. G. simulated XRD pattern; P. P. and N. L. performed the CL measurements and relative analysis was performed by P. P., N. L., and P. D. P.; P. D. P., B. O., R. S., F. M. C da S., H. C. N. T., performed XRF at CARNAUBA, beamline LNLS, Sirius, and relative analysis. P. D. P., B. O., T. C. R. da R., L. G. de F. B.,F. C. V. performed photoemission at IPE beamline, at LNLS, Sirius, and relative analysis.. P. D. P. wrote the original draft., and C. O., A. D. C., S. C., A. D. P., A. P., B. P., P. P., N. L. helped to review the manuscript. P. D. P., and A.D.C. secured funding. All authors contributed to the discussion of results and the final manuscript preparation.

Competing interests

The authors declare no competing interests.

Additional information

Supplementary information The online version contains supplementary material available at https://doi.org/10.1038/s43246-026-01261-3.

Correspondence and requests for materials should be addressed to Paola De Padova.

Peer review information *Communications Materials* thanks Junsheng Chen and the other, anonymous, reviewer(s) for their contribution to the peer review of this work.

Reprints and permissions information is available at http://www.nature.com/reprints

Publisher's note Springer Nature remains neutral with regard to jurisdictional claims in published maps and institutional affiliations.

Open Access This article is licensed under a Creative Commons Attribution-NonCommercial-NoDerivatives 4.0 International License, which permits any non-commercial use, sharing, distribution and reproduction in any medium or format, as long as you give appropriate credit to the original author(s) and the source, provide a link to the Creative Commons licence, and indicate if you modified the licensed material. You do not have permission under this licence to share adapted material derived from this article or parts of it. The images or other third party material in this article are included in the article's Creative Commons licence, unless indicated otherwise in a credit line to the material. If material is not included in the article's Creative Commons licence and your intended use is not permitted by statutory regulation or exceeds the permitted use, you will need to obtain permission directly from the copyright holder. To view a copy of this licence, visit http://creativecommons.org/licenses/by-nc-nd/4.0/.

© The Author(s) 2026